Layer 6 corticocortical cells dominate the anatomical organization of intra and interhemispheric feedback

Simon Weiler[1], Manuel Teichert[2,3], and T. W. Margrie[1,3]

[1] *Sainsbury Wellcome Centre for Neuronal Circuits and Behavior, University College London, 25 Howland Street, London W1T 4JG, United Kingdom*
[2] *Jena University Hospital, Department of Neurology, Am Klinikum 1, 07747 Jena, Germany*
[3] *These authors contributed equally*

Abstract

The mouse neocortex contains at least ninety functionally distinct areas that are symmetrically located across the two hemispheres. Determining the logic of this long range circuitry is necessary for understanding how inter-areal cortical integration enables high level brain function involving multiple sensory, motor and cognitive processes. To address this we have performed a systematic anatomical analysis of the areal and laminar organization of the ipsilateral and contralateral cortical projection onto the primary visual (VISp), primary somatosensory barrel field (SSp-bfd) and primary motor (MOp) cortices. The resultant input maps reveal that although the ipsilateral hemisphere is the major source of cortical input, there is substantial bilateral symmetry regarding the relative contribution and areal identity of cortical input. Laminar analysis of these input areas show that intra and interhemispheric connectivity is mediated predominantly by excitatory Layer 6 corticocortical cells (L6 CCs). Based on cortical hierarchy analysis that compares the relative contribution of inputs from supra- (feedforward) and infra-granular (feedback) layers, we find that contra-hemispheric projections reflect a dominant feedback organization compared to their ipsi-cortical counterpart, independent of the target injection area. The magnitude of the interhemispheric difference in hierarchy was largest for sensory and motor areas compared to frontal, medial or lateral brain areas and can be explained by a proportional increase in input from L6 projection neurons. L6 CCs therefore not only dominate corticocortical communication but also reflect its inherent feedback organization.

Keywords: Cortical projectome, Interhemispheric, Layer 6, Anatomical hierarchy, Sensory-motor

1 Introduction

The cortex is divided into two hemispheres that do not function independently. Rather, they are connected by commissural fibers, most notably the corpus callosum which is thought to coordinate function across the brain (Gazzaniga 2000; Zhou *et al.* 2013; Innocenti *et al.* 2022; Ocklenburg and Guo 2024). Within these circuits feedforward and feedback pathways represent two fundamental types of information flow (Berezovskii, Nassi, and Born 2011; Markov *et al.* 2013). In the case of sensory processing, feedforward connections typically carry sensory input towards areas higher in cortical hierarchy where more complex processing occurs (Rockland and Pandya 1979; Felleman and Van Essen 1991; Mumford 1992; Siegle *et al.* 2021). Conversely, cortical feedback typically originates in higher-order areas and projects back to brain areas of lower hierarchical rank (Rockland and Pandya 1979; Felleman and Van Essen 1991; Markov and Kennedy 2013). These pathways are believed crucial for modulating sensory processing, enhancing signal fidelity, integrating contextual information and forming predictions (Rao and Ballard 1999; Xu *et al.* 2012; Zhang *et al.* 2014; Leinweber *et al.* 2017; Keller and Mrsic-Flogel 2018; Marques *et al.* 2018; Weiler *et al.* 2024; Teichert and Bolz 2018).

The mammalian neocortex contains up to six layers that play distinct roles in feedforward and feedback processing (Markov *et al.* 2013; Markov *et al.* 2014; Harris *et al.* 2019). For instance,

bioRxiv (2024)

Corresponding author
TW Margrie t.margrie@ucl.ac.uk

© The Authors 2024. Published on bioRxiv.

retrograde tracing (Markov *et al.* 2014) and physiological analysis (Buffalo *et al.* 2011; Bastos *et al.* 2015) in the visual cortical system of primates indicate that supragranular layers are the main source of feedforward projections while infragranular layers are the main source of feedback input. Moreover, the ratio of supra- to infra-granular layer projections has been used to reveal the anatomical basis of visual cortical hierarchy in primates and mice (Barone *et al.* 2000; Markov *et al.* 2014; D'Souza *et al.* 2022; Yao *et al.* 2022). While it is established that functional cortical hierarchy (at least in the visual system) reflects the laminar organization of cortical input within the ipsilateral hemisphere, it remains unknown how this is combined or even reflects the organization of input from the contralateral hemisphere. More specifically, to date there remains no cortex-wide anatomical analysis that investigates the nature of circuit hierarchy onto a given area that arises from both hemispheres. Also, which cortical layers are responsible for the establishment of the intra versus the interhemispheric cortical hierarchy is not understood.

In this study, we utilized state of the art retro-AAV based neuronal tracing in adult mice to detect the nuclei of projection neurons and map the cortex-wide projectome onto the primary visual cortex (VISp), primary somatosensory barrel field (SSp-bfd) and the primary motor cortex (MOp). We employ an anatomically based hierarchy metric that not only enables us to define the contribution of L2/3 and the infragranular layers but also enables us to disassociate the roles of L5 and L6 in the organization of the feedback circuits that mediate corticocortical communication. Our results indicate extensive and symmetric interconnectivity across both hemispheres and reveal a key role for L6 in mediating cortical feedback within and across the two hemispheres.

2 Results

To systematically map the cortical projections onto primary sensory and motor cortical areas in adult mice, we utilized retrograde tracing with a recombinant AAV-variant, AAV-EF1a-H2B-EGFP (nuclear retro-AAV), which is taken up by axon terminals (Tervo *et al.* 2016) and results in EGFP expression in the nuclei of projection neurons (Fig. 1A, Fig.S1A). This tracer was injected in either the primary visual cortex (VISp, n = 6), the barrel field of the primary somatosensory cortex (SSp-bfd, n = 6) or the primary motor cortex (MOp, n = 6), whereby each mouse received a single injection, spanning across all cortical layers of each target area (Fig. 1A, Fig.S2-S3). Following ex-vivo two-photon tomography (Ragan *et al.* 2012), 3D cell detection (Tyson *et al.* 2021) identified nucleus-labeled neurons and assigned them to cortical areas of the Allen Mouse Brain Common Coordinate Framework (Wang *et al.* 2020; Claudi *et al.* 2020, CCFv3, Fig. 1B, excluding the targeted injection area). We found that the vast majority of projection neurons (99%) to all target areas were not overlapping with GAD-expressing cells (Fig.S4A). Regarding L6 projection neurons, they were also found to be non-overlapping with NTSR1-expressing corticothalamic cells and therefore indicative of L6 CCs (Fig.S4B,C).

The areal organization of cortical input to VISp, SSp-bfd and MOp Our analysis revealed that tracer injections into VISp, SSp-bfd, and MOp resulted in the labeling of several hundred thousand projection neurons throughout both hemispheres of the cerebral cortex (Fig.S1B), with approximately 80% located ipsilateral and 20% contralateral to the injection site (Fig. 1B,C, $p<0.05$, two-sided Wilcoxon signed-rank test). While all three target areas received ipsilateral input from almost all 45 cortical areas (VISp, range: 41 - 44, n = 6; SSp-bfd, range: 43 - 44, n = 6, MOp, range: 33 - 39, n = 6, Fig. 1D) the two sensory cortical targets received input on average from more areas than the primary motor cortex (Fig. 1D, sensory = 43.58 ± 0.26, n = 12 versus motor 36.67 ± 0.99, n = 6; $p<0.001$, two-sided Wilcoxon rank-sum test). Comparing the inputs from both hemispheres showed that VISp and MOp injections revealed asymmetry in the number of areas labeled per hemisphere (Fig. 1D, VISp ipsilateral = 43.33 ± 0.49 versus VISp contralateral 38.33 ± 0.72, MOp ipsilateral = 36.67 ± 0.99 versus MOp contralateral 30.67 ± 0.67, $p<0.05$, signed-rank test), whereas the source of input to SSp-

bfd appeared to be mirrored across the two hemispheres (Fig. 1D, SSp-bfd ipsilateral = 43.83 ± 0.17 versus SSp-bfd contralateral 42 ± 1.61, p=0.5, two-sided Wilcoxon signed-rank test). Importantly, we found there to be no instance where a projection area in the contralateral hemisphere did not have an ipsilateral counterpart. These data show that both primary sensory and motor cortices receive an abundance of functionally diverse input from cortical areas outside the counterpart (homotopic) contralateral area indicating significant crossmodal integration within and between the two hemispheres (Fig. 1E).

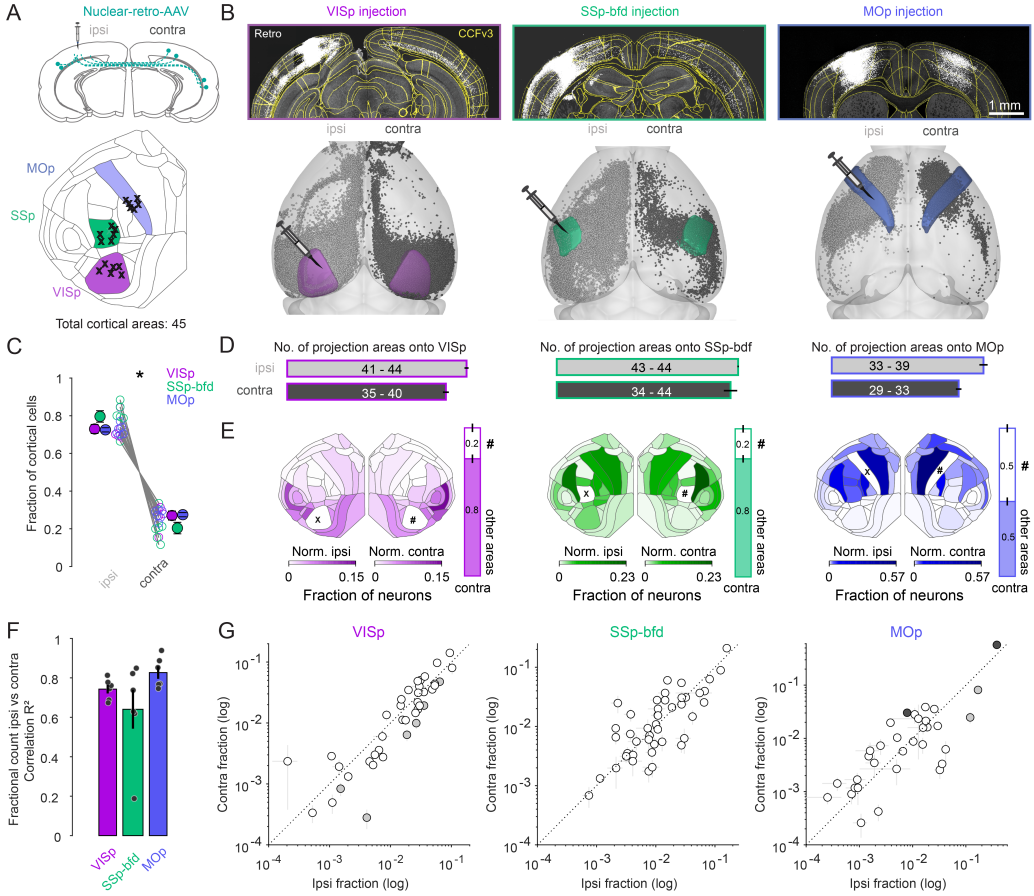

Figure 1. Widespread and bilaterally symmetrical cortical projections to VISp, SSp-bfd and MOp. (A) Retrograde nuclear retro-AAV was injected across all layers of the primary visual cortex (VISp), somatosensory barrel field (SSp-bfd) and the motor cortex (MOp) of mice. The locations of the centroids on the injection bolus is shown on the CCFv3 cortical flat map. Injections performed in the right hemisphere injection (n = 11) are flipped to their corresponding location in the left hemisphere. (B) Two photon images showing examples of injection sites and labeled nuclei of retro-AAV labeled cells. Visualization of detected projection neurons for three individual mice warped into the 3D rendered space of the two hemispheres. (C) Plot showing the fraction of cortical cells per hemisphere detected for each mouse and pooled according to each injection site (mean ± sem). Asterisks indicate statistical significance ($p < 0.05$). (D) Bar graphs indicating the mean number (± sem) of cortical areas in which labeled neurons were observed. Text indicates the range of areas. (E) Flat maps indicating the relative cell counts normalized for each hemisphere excluding both the injection target (X) area its homotopic counterpart (#). Right, Bar graphs indicating the fraction of cells in the contralateral hemisphere located in the homotopic versus all other cortical areas (mean ± sem). Note that areas ILA (5), ENTl (44) and ENTm (45) are not represented in the cortical flat map on the left (see also Fig.S1C). (F) Bar graphs showing the average correlation (R^2 ± sem) of the ipsi- versus contra-lateral fractional count superimposed on the individual R^2 values for each experiment. (G) Plot of the ipsi- versus contra-lateral fractional count for each of the three target areas. Each circle represents the average of six fractional count values (± sem) for a given area. Open circles indicate instances where the difference of the ipsilateral values are not significant from the contralateral values. Black circles indicate a significant contralateral bias while gray circles indicate an ipsilateral bias. Dashed line indicates the unity line.

To understand the relative contribution of a given area to the projectome for each hemisphere we performed a correlation analysis on the relative fraction of labeled cells per area normalized to the total hemispheric count. Excluding the homotopic target area, which always contained the highest fraction of cells, but including all the cases where the number of cells in an area exceed ten in three or more mice (see Methods), we found a strong correlation between the fractional count of neurons in a given ipsilateral brain area with its contralateral counterpart (VISp $R^2 = 0.74 \pm 0.02$, $p<0.05$; SSp-bfd $R^2 = 0.64 \pm 0.1$, $p<0.05$; MOp $R^2 = 0.83 \pm 0.03$, $p<0.05$, linear regression fit, Fig. 1E,F). This relationship was observed independent of the target identity (Fig. 1F,G). When directly comparing the relative projection weights of the individual cortical areas from the two hemispheres, we found that 34, 44 and 29 out of 44 areas (VISp, SSp-bfd, MOp, respectively) were not significantly different from one another which indicates significant bilateral symmetry in the relative contribution of a given area to its hemispheric projectome (Fig. 1G, individual one-sample t-tests on contra-ipsi difference, Bonferroni multiple comparison correction).

Based on their degree of inter-areal cortical connectivity it has been suggested that the mouse neocortex consists of six anatomical modules referred to as prefrontal, lateral, somatomotor, visual, medial and auditory (Fig. 2A, Harris *et al.* 2019). To determine whether the areal projections reflect any underlying modular organization we next analyzed the distribution of projection neurons according to their respective module. Firstly, while the VISp target projection was heavily dominated by input from the visual module (Fig. 2B, ipsilateral visual module fractional count 0.42 ± 0.02 versus medial module 0.15 ± 0.02; contralateral visual module 0.42 ± 0.03 versus lateral module 0.22 ± 0.02, $p<0.001$, two-sided unpaired t-test), both the SSp-bfd and MOp targets received input predominantly from the somatomotor module (Fig. 2B, SSp-bfd: ipsilateral somatomotor module fractional count 0.62 ± 0.05 vs. visual module 0.16 ± 0.03, contralateral somatomotor module 0.53 ± 0.02 versus lateral module 0.24 ± 0.02, $p<0.001$; MOp: ipsilateral somatomotor module 0.83 ± 0.02 versus prefrontal module 0.08 ± 0.02, contralateral somatomotor module 0.71 ± 0.03 versus lateral module 0.14 ± 0.01, $p<0.001$, two-sided unpaired t-test). For both the visual module projection to VISp and the somatomotor module projections to SSp-bfd and MOp there were similar contributions from the majority of the underlying areas (Fig. 2C). Secondly, although both VISp and SSp-bfd received significant input from all modules in both hemispheres, we find there to be almost no input onto MOp from the visual, auditory and medial modules in either hemisphere (Fig. 2B, less than 0.01 fractional count for each of these three modules). Finally, there also appears to be biases in the relative density of projections. For example, as it has been previously shown (Yao *et al.* 2022), we find that the lateral module in the contralateral hemisphere projecting to VISp is more strongly weighted than its ipsilateral counterpart and that this driven primarily by the connection from the temporal association area (TEa) and ectorhinal cortex (ECT) (Fig. 2B,C, lateral module ipsilateral 0.19 ± 0.02 vs. contralateral 0.22 ± 0.02, $p=0.05$, one-tailed paired t-test). While this contralateral dominance of the lateral module also emerges from the projection profiles to SSp-bfd and MOp it is rather mediated by many, albeit less dominant, lateral module areas (Fig. 2C, SSp-bfd: lateral module fractional count ipsilateral 0.1 ± 0.01 versus contralateral 0.24 ± 0.02, $p<0.001$, one-tailed paired t-test, MOp: lateral module ipsilateral 0.08 ± 0.01 versus contralateral 0.14 ± 0.01, $p<0.01$, one-tailed paired t-test).

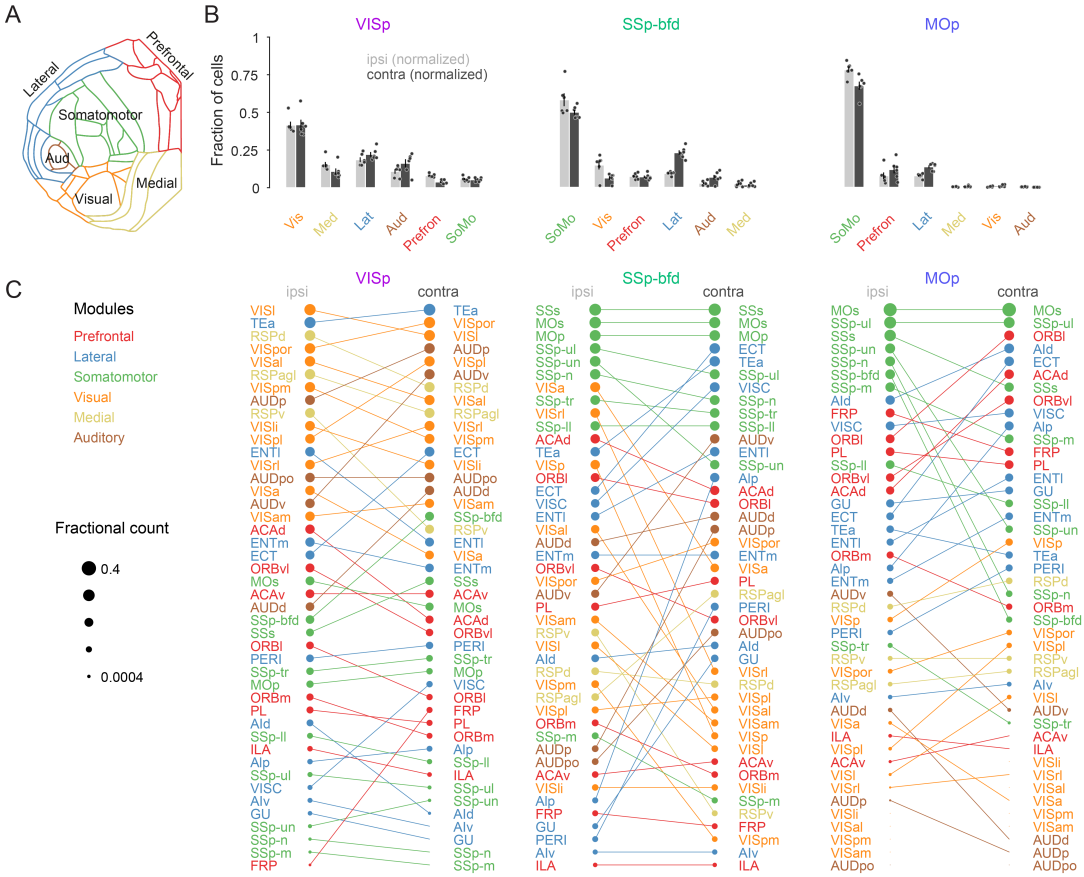

Figure 2. Modular organization of the intra and interhemispheric projection onto VISp, SSp-bfd and MOp (A) Schematic of the cortical flat map highlighting the six cortical modules and their corresponding areas. (B) Bar graphs of the normalized fractional cell counts for each of the six modules for ipsilateral and contralateral hemispheres ranked by decreasing ipsilateral weights. For the contralateral hemisphere the homotopic target region is not included. (C) Rank plot based on the relative weights of connectivity onto the target areas VISp, SSp-bfd and MOp for all cortical brain areas. The size of the circle indicates relative fractional count on a logarithmic scale. Corresponding areas on the ipsilateral and contralateral hemisphere are connected with a line.

The laminar organization of cortical input to VISp, SSp-bfd and MOp Next, we asked whether there were specific subsets of projection neurons that might differentially contribute to the local and global projection by quantifying the distribution of neurons across all cortical layers in both hemispheres (Fig. 3A1-A4). Firstly for each injection target we find that the majority of detected neurons were located in L2/3, L5, and L6a (Fig. 3B) with a very low fraction of labeled neurons in L4 and L6b. To begin to explore the laminar structure in the input to the three target areas we next compared the relative dominance of these three main layers. Regardless of hemisphere, L2/3 was found not to be the dominant layer of inter-areal input (Fig. 3C1,C2,D1,D2). For VISp and MOp L6 dominated both the intra and interhemispheric projection (Fig. 3C1,C2,D1,D2, $p<0.01$, one-way ANOVA, Tukey-Kramer multiple comparison correction). In the case of SSp-bfd L5 and L6 dominated the contralateral input (Fig. 3C2,D2) and shared dominance with L2/3 only for the ipsilateral projection (Fig. 3C1,D1). When pooled, we find that the majority of projection source areas display L6 dominance, followed by L5 with only a small fraction of areas exhibiting L2/3 dominance (Fig. 3E, $p<0.05$, one-way ANOVA, Tukey-Kramer multiple comparison correction). These data show that L6 is a key player mediating intra and interhemispheric connectivity onto primary sensory and motor areas.

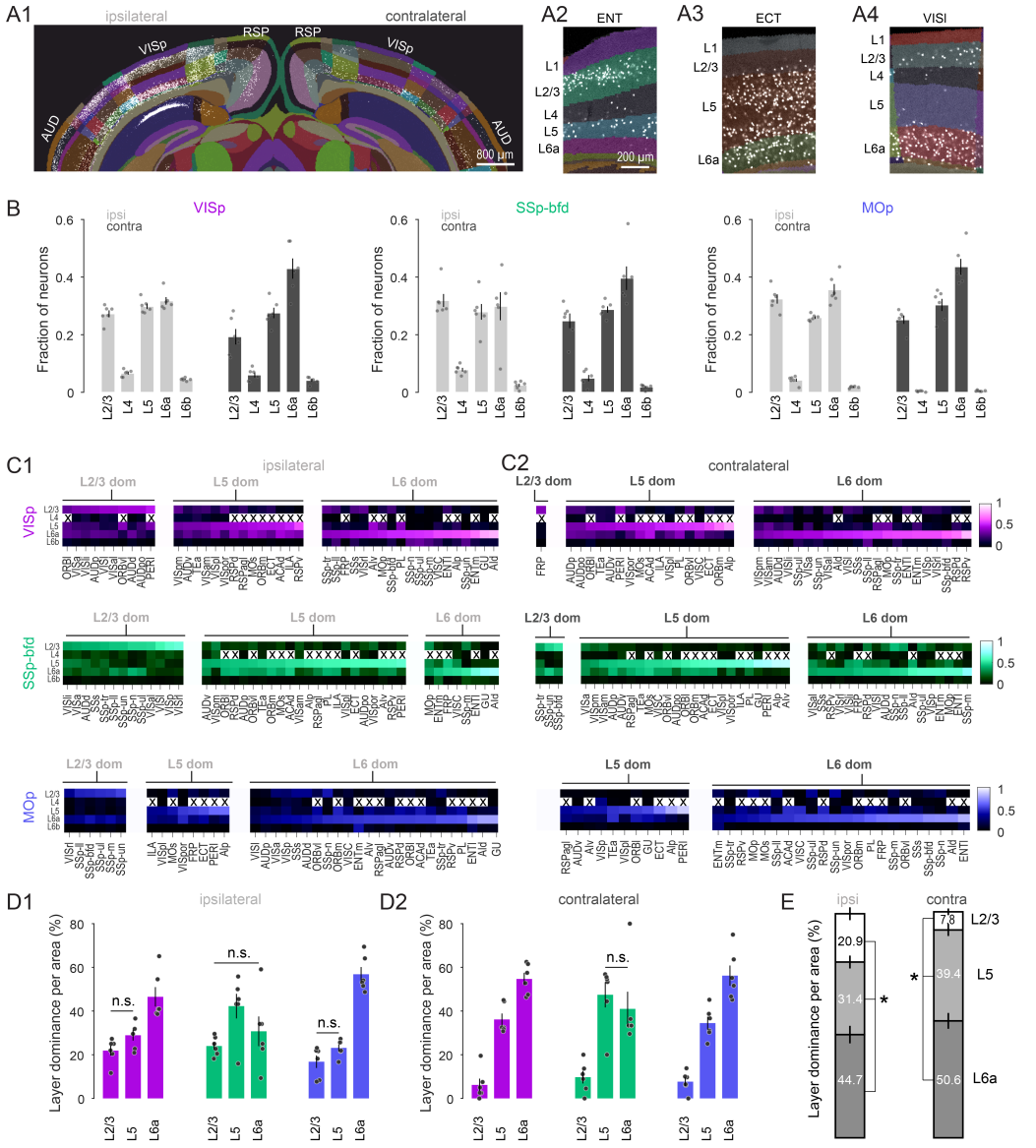

Figure 3. Layer 6 is a main source of input to VISp, SSp-bfd and MOp. (A1) A segmented image of the cortex used to assign the laminar position of detected neurons. Image of segmented Enthorinal (ENT), Ectorhinal (ECT), and lateral visual area (VISl) on the contralateral hemisphere showing local dominance by L2/3 (A2), L5 (A3) and L6a (A4), respectively. (B) Bar plot showing average fraction of cells (± sem, n = 6 mice) in L2/3, L4, L5, L6a and L6b across the ipsilateral and contralateral hemisphere for the three injection targets. (C) Average heat maps (n = 6 mice) based on the fractional count across laminae for each cortical area separated according to injection target and local dominance for ipsilateral (C1) and contralateral (C2) hemispheres. Dominance quantification is based on average laminar fractional count across animals. Crosses indicate cortical areas that do not contain L4. (D) Bar graphs showing the average percentage of areas (± sem, n = 6 mice) in which L2/3, L5 and L6 dominate the fractional cell count for ipsilateral (D1) and contralateral (D2) hemispheres. Unless indicated, all comparisons reach statistical significance (n.s. = non-significant). Dominance quantification is based on laminar fractional count per animal. (E) Stacked bar plots showing average laminar dominance for all cortical areas (± sem) pooled across all injection targets. Asterisks indicate statistical significance ($p < 0.05$).

Contralateral input onto VISp, SSp-bfd and MOp displays high cortical hierarchy In primates, the laminar distribution of projection neurons has been used to interpret the degree to which cortico-cortical networks might be feedforward or feedback (Barone *et al.* 2000; Markov *et al.* 2014; Vezoli *et al.* 2021). A predominance of incoming projection neurons from supragranular layers (L2/3) signifies a feedforward connection, whereas a higher proportion in infragranular layers (layers 5

and 6) is considered to reflect a feedback projection (Fig. 4A). Additionally, cortical areas with a higher proportion of projection neurons in infragranular, compared to supragranular layers, are suggested to have a higher hierarchical rank (Fig. 4A, Markov *et al.* 2014; Barone *et al.* 2000; Vezoli *et al.* 2021). Thus, the hierarchical rank of a specific projection area can be estimated by calculating the fraction of infragranular labeled neurons (fILN) (Fig. 4A,B). Previously in the mouse visual cortex, similar anatomical measures of hierarchy have been performed using anterograde tracers (D'Souza *et al.* 2022) and modified retrograde rabies virus (Yao *et al.* 2022) to identify either target lamina or presynaptic cell populations. Using retrograde AAV-EF1a-H2B-EGFP and by detecting EGFP expression in the nuclei of projection neurons we find a very similar hierarchical ranking of the higher cortical visual areas as previously shown (Fig.S5, Yao *et al.* 2022; D'Souza *et al.* 2022).

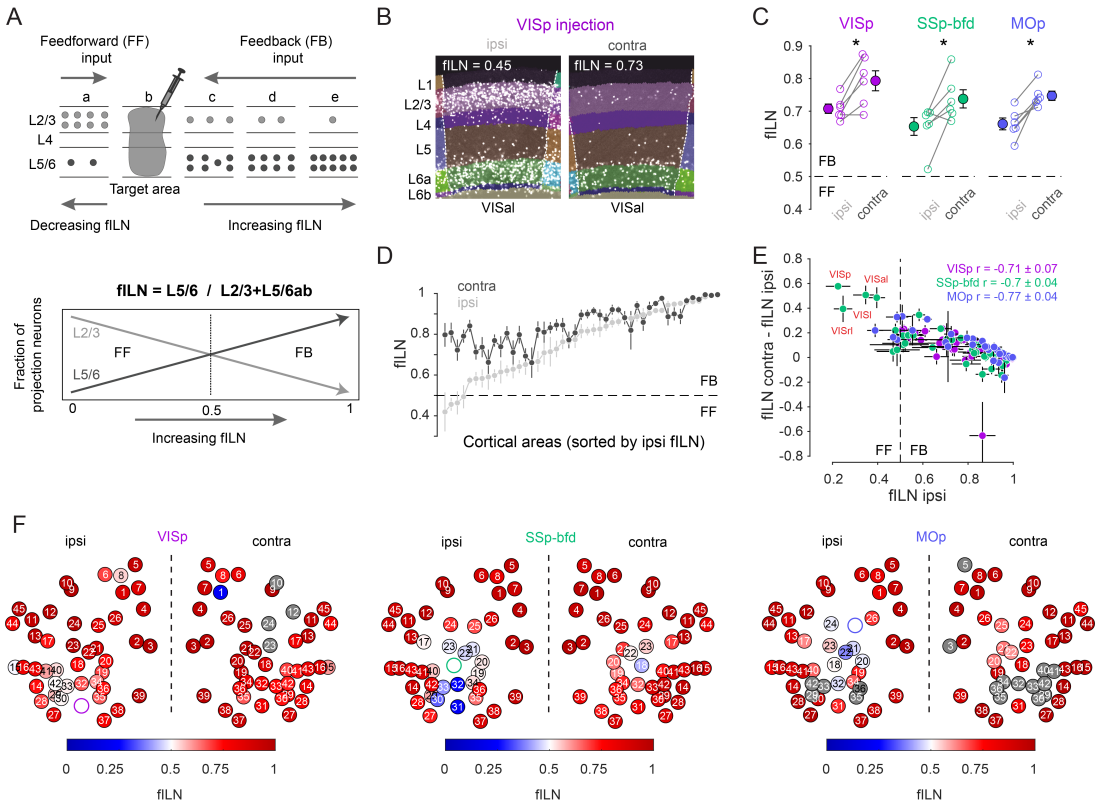

Figure 4. Cortical hierarchy onto VISp, SSp-bfd and MOp. (A) Cartoon showing the laminar basis of the anatomical determination of cortical hierarchy (Top). As the fraction of supragranular (L2/3) neurons decrease and/or the number of L5 and L6 neurons increase, the proportion of infragranular neurons (fILN) increases reflecting a predominance of feedback input (Bottom). (B) Segmented image of the ipsilateral and contralateral anterolateral visual area (VISal) projecting onto VISp showing the laminar position of detected cells. (C) Plots showing fILN values for all neurons within each hemisphere (blind to individual cortical areas) for each mouse for the three target injections. Average fILN values (± sem) are depicted by filled circles. (D) Plot showing the average fILN values (± sem) for each of the 45 areas (pooled across different injection experiments) and ranked according to the ipsilateral fILN values. (E) Scatter plot showing the correlation between the ipsilateral fILN values and the difference between the contralateral and ipsilateral fILN values for the three target injections. Average correlation values (± sem, n = 6 mice) for each target area are displayed (top right). Highlighted in red are the primary (VISp), rostrolateral (VISrl), lateral (VISl) and anterolateral (VISal) visual areas projecting to SSp-bfd that display low ipsilateral fILN and high contralateral fILN values. (F) Heatmap plot displaying the ipsilateral and contralateral fILN values for each cortical brain area for the three injection targets. Open circles denote injection areas. Gray circles indicate cortical areas with no projections to VISp, SSp-bfd or MOp. Numbers 1-45 indicate different brain areas, see Fig. S1.

Independent of the injected target area, the average fILN for both hemispheres indicates that cortical input onto VISp, SSp-bfd and MOp reflects predominantly a feedback organization (Fig. 4C).

However, on average, and compared to the ipsilateral projection, the average fILN of the contralateral hemisphere is larger across all injection targets (Fig. 4C, $p<0.05$, one-sided paired t-test, respectively). Moreover, the overall contralateral input appears more narrowly distributed in its anatomical organization, maintaining relatively high fILN values across all brain areas (Fig. 4C,D; fILN range ipsilateral: 0.42 ± 0.1 - 1.0 ± 0.0 versus contralateral: 0.66 ± 0.07- 1 ± 0). As a consequence, regardless of the target area, we found a strong significant negative correlation between the areal fILN values on the ipsilateral side and the magnitude of the difference in the fILN of their contralateral counterpart (Fig. 4E, VISp: r = -0.71 ± 0.07, SSp-bfd: r = -0.7 ± 0.04, MOp: r = -0.77 ± 0.04, $p<0.05$, Spearman correlation). In line with the classical view of reciprocal feedforward/feedback connectivity (Markov *et al.* 2014; Young *et al.* 2021; Angelucci and Petreanu 2023) and in the case where we can directly compare the interconnectivity of two target sources within the ipsilateral hemisphere (VISp and SSp-bfd), we see feedforward input from VISp to SSp-bfd and feedback input from SSp-bfd to VISp (Fig. 4F, Fig.S6A,B, magenta and green arrow). However, all contralateral areas were found to provide predominantly feedback input (Fig. 4D,F, Fig.S6A-C, Fig. 4D). These correlations also reveal unique instances, for example in SSp-bfd, where the ipsilateral and contralateral input from a subset of visual areas showed opposing signatures in their anatomical organization. Ipsilateral mediating feedforward while contralateral providing feedback input (highlighted in red in Fig. 4E, Fig. 4F, Fig.S6A-C). Together, these data show that input onto these primary sensory and motor areas is mediated largely by a high proportion of L5 and L6 neurons and that both ipsilateral and contralateral input is predominantly feedback (Fig. 4F). However, in some instances ipsilateral input can appear strongly feedforward and in stark contrast to the feedback organization of projections from the same area in the contralateral hemisphere.

Increased contralateral hierarchy is due to differences in the laminar organization of sensory and motor input Within the ipsilateral hemisphere, anterogradely labeled sensory-motor module projections have been shown to exhibit low hierarchy compared to lateral, medial and prefrontal modules (Harris *et al.* 2019). Using retrograde tracing and our fILN measure we find this to be the case not only for the ipsilateral hemisphere but also for the contralateral hemisphere (Fig. 5A). Strikingly, ranking cortical modules according to their fILN values revealed extremely similarly high levels of feedback from prefrontal, medial and lateral modules (pf-m-l) from both hemispheres. In contrast, the fILN values for visual, auditory and somatomotor (v-a-sm) modules were different across the two hemispheres (Fig. 5A,B) with the contralateral hemisphere providing much stronger feedback (Fig. 5A,B, ipsilateral fILN 0.65 ± 0.02 versus contralateral fILN 0.79 ± 0.01, $p<0.001$, two-sided paired t-test). The difference between the ipsilateral and contralateral fILN was also significantly larger for the v-a-sm compared to the pf-m-l module when the data was partitioned according to the target areas (Fig. 5C, $p<0.001$, one-sided paired t-test). Therefore, this appears to be another generalizable principle concerning the organizational hierarchy onto the primary sensory and motor cortices. Moreover, these results suggest that the global differences in the fILN between the two hemispheres observed above are mainly due to hemispheric differences in the fILN between the v-a-sm modules.

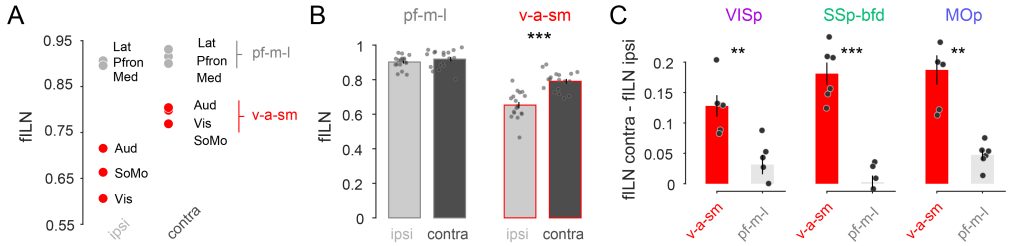

Figure 5. Sensory and motor but not lateral, prefrontal and medial projections explain asymmetric cortical hierarchy. (A) Plot showing the average fILN values for all areas in a given module for n = 18 mice irrespective of target area. Red circles indicate the sensory and motor modules (visual, auditory and somatomotor; v-a-sm) while grey circles indicate prefrontal, medial and lateral (pf-m-l) modules. (B) Bar graphs comparing cross hemispheric fILN values (mean ± sem) for prefrontal, medial and lateral (pf-m-l) and sensory and motor (v-a-sm) modules. Each circle represents a single animal (n = 18). (C) Bar graphs (mean ± sem) showing the interhemispheric difference in fILN values between the two modular groupings for each target projectome. Each circle represents a single animal (n = 6, respectively).

L6 accounts for the hierarchical organization of intra and interhemispheric corticocortical feedback. Finally we sought to determine which cortical layers within the v-a-sm module might account for the comparatively high contralateral fILN values. There are at least three possible scenarios that could give rise to high fILN values. Theoretically, increased fILN can stem from a reduction in the proportion of projection neurons located within L2/3, an increase in the proportion of projection neurons within L5/6, or a synergistic effect involving opposing changes in supra- and infra-granular layers (Fig. 6A). By pooling all areas (n = 24) within the three key sensory and motor modules for the contralateral side we observe a significant reduction in L2/3 neurons for all target areas (Fig.6B, ipsilateral versus contralateral L2/3 fractional counts: VISp 0.25 ± 0.02 versus 0.15 ± 0.02, SSp-bfd 0.36 ± 0.02 versus 0.22 ± 0.03, MOp 0.23 ± 0.01 versus 0.1 ± 0.01, $p<0.001$, one-sided paired t-test) and a concomitant increase in L6 cells in VISp and SSp-bfd (Fig. 6B, ipsilateral versus contralateral L6 fractional counts: VISp 0.38 ± 0.02 versus 0.42 ± 0.01, SSp-bfd 0.24 ± 0.04 versus 0.4 ± 0.01, $p<0.05$, one-sided paired t-test). We found there to be no change in the fraction of L5 neurons between the ipsilateral and contralateral hemispheres (Fig. 6B, ipsilateral versus contralateral L5 fractional counts: VISp 0.19 ± 0.02 versus 0.21 ± 0.01, $p = 0.38$; SSp-bfd 0.27 ± 0.04 versus 0.28 ± 0.01, $p = 0.86$; MOp 0.13 ± 0.02 versus 0.12 ± 0.2, $p = 0.24$, two-sided paired t-test).

We therefore next compared the fraction of projection neurons in a given layer to its counterpart area and layer to identify which areal subpopulations of cells might be responsible for the observed global laminar differences in the fILN (Fig. 6C). We find there to be many areas where L2/3 is significantly decreased and where L6 is increased. L5 was more heterogeneous containing instances of both decreases and increases in the average fraction of labeled cells between the two hemispheres (Fig. 6C). Taking only those areas where we observed a significant change in the fraction of L2/3, L5 or L6 cells we found that, depending on the target area, thirty to sixty percent of sensory-motor areas showed a dramatic reduction in the fraction of contralaterally-labeled L2/3 neurons. In contrast, between thirty to fifty percent of areas showed increases in contralateral L6 cells. On the other hand, L5 showed the most balanced changes since its fractional contribution generally both increased and decreased depending on the target area (Fig. 6D). These data show that increased fILN in the contralateral hemisphere is due to an abundance of L6 cells and indicates their key role in interhemispheric feedback. To test for the importance of L6 in the establishment of both the ipsilateral and contralateral hierarchies and the difference between the two (Fig. 6D), we excluded L6 from the fILN calculation (Fig. 6A). First, by comparing the default ipsilateral fILN values for all cortical areas located within the v-a-sm modules to those when L5 or L6 was excluded, we observe significant changes in fILN (Fig. 6E, $p<0.001$, two-sided paired t-test, Bonferroni multiple comparison correction).

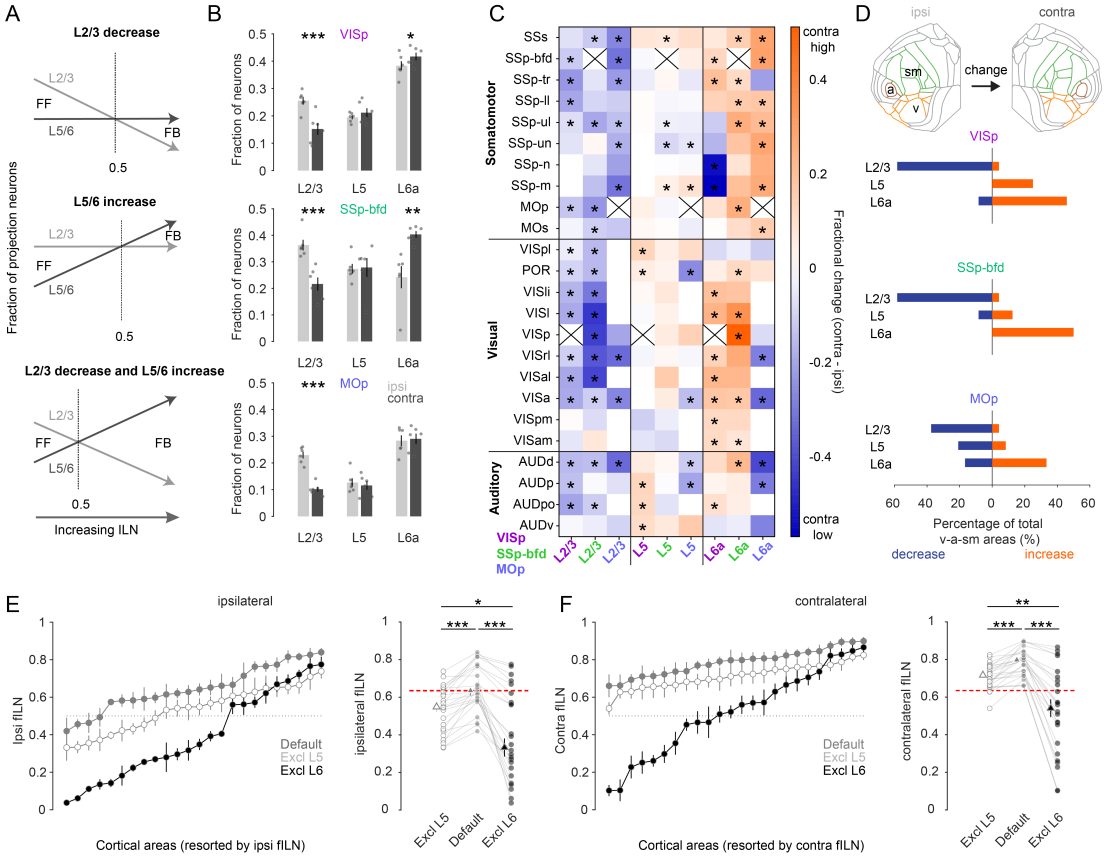

Figure 6. L6 dominates cortical hierarchy in sensory and motor areas within and between the two hemispheres. (A) Schematic illustrating at least three hypothetical ways in which changes in the relative distribution of L2/3, L5 and L6 neurons can give rise to increases in the fILN and reflect a predominantly feedback network. (B) Bar graphs showing the average (± sem) normalized fractional count (excluding L4 and 6b) of cells for the sensory and motor modules projecting to each target area from both hemispheres (ipsi, gray; contra, black), (C) Heat map displaying the fractional change of projections for L2/3, L5 and L6a between the contralateral and ipsilateral hemisphere. Displayed are the 24 individual brain areas in the sensory and motor modules for the three target areas VISp, SSp-bfd and MOp. Asterisks denote areas that significantly change between the ipsilateral and the contralateral hemispheres. Crosses indicate excluded homotopic areas. (D) Flat map indicating the three sensory and motor modules (top). Stacked horizontal bar plots displaying the percentage of the total number cortical areas in the sensory and motor modules that significantly decrease (blue) or increase (orange; indicated by the asterisks in C) for the three target areas. (E) (Left) Plots showing the average fILN (± sem) for each sensory and motor area (pooled across all target areas, n = 18 mice) and ranked according to the ipsilateral values for the default network (gray filled circles), the default network excluding L5 (open circles) and the default network excluding L6 (black filled circles). (Right) Scatter plots showing the average ipsilateral fILN scores for each of the twenty four areas of the default network, the default network excluding L5 and the default network excluding L6. Filled triangles represent the mean (± sem) of the average fILN values. Red line indicates the mean of the ipsi default network. (F) (Left) Plots showing the average fILN (± sem) for each sensory and motor area (pooled across all target areas, n = 18 mice) and ranked according to the ipsilateral values for the default network (gray filled triangles), the contralateral values for the default network (gray filled circles), the contralateral values for the default network excluding L5 (open circles) and the default network excluding L6 (black filled circles). (Right) Scatter plots showing the average fILN scores for each of the twenty four areas of the ipsi and contra default network, the default contra network excluding L5 and the default contra network excluding L6. Filled triangles represent the mean (± sem) of the average fILN values. Red line indicates the mean of the ipsi default network.

Importantly, the reduction in ipsi fILN was greatest when L6 was excluded compared to L5 (Fig. 6E, $p<0.05$, one-sided paired t-test, Bonferroni multiple comparison correction). This was also observed when performing the same comparisons on the default contralateral fILN (Fig. 6F). Excluding L6 from the contralateral default network actually had such a significant impact that the resultant fILN was substantially lower than the default ipsilateral side (Fig. 6F, default fILN ipsilateral 0.65 ± 0.03 vs. fILN contra excluding L6 0.52 ± 0.05, $p<0.05$, one-sided paired t-test, Bonferroni multiple comparison correction). These data show that L6 exerts a major influence on the anatomical organization of cortical input onto VISp, SSp-bfd and MOp and accounts for the differences in the feedback hierarchy observed within and between the two hemispheres.

3 Discussion

By performing comprehensive bilateral cortical circuit mapping onto VISp, SSp-bfd and MOp we find that both primary sensory and motor areas receive extensive input from the majority of areas not only located in the ipsilateral (Ährlund-Richter *et al.* 2019; Hafner *et al.* 2019; Sun *et al.* 2019; Brown *et al.* 2021; Muñoz-Castañeda *et al.* 2021; Yao *et al.* 2022) but also contralateral cortical hemisphere (Goulas, Uylings, and Hilgetag 2017; Yao *et al.* 2022). This indicates significant cross-modal interactions not only within but also between the two cortical hemispheres. With only a few exceptions, we find that the identity of input sources is mirrored across the two hemispheres and displays bilateral symmetry in their relative projection weights. One such exception relates to the contralateral lateral module whose composite cortical areas, compared to the ipsilateral module, display a stronger connection onto VISp (Yao *et al.* 2022), SSp-bfd and MOp indicating it may be a unique but generalisable feature of interhemispheric connectivity.

Earlier studies indicate that input from the other hemisphere onto a given area arises primarily and almost exclusively from the same contralateral area (Yorke Jr. and Caviness Jr. 1975; Zhao, Liu, and Cang 2013; Fenlon and Richards 2015). While we find many labeled cells in the contralateral target area, our data indicate that heterotopic connections are a prominent anatomical feature of the interhemispheric network (Goulas, Uylings, and Hilgetag 2017; Swanson, Hahn, and Sporns 2017; Yao *et al.* 2022; Szczupak *et al.* 2023). For both primary sensory areas the majority of the contralateral input comes from heterotopic areas located within target areas' home module followed by areas located within most of the remaining modules. In contrast, MOp appears to receive very little input from areas relating to medial, visual and auditory modules.

Neurons projecting from the contralateral hemisphere are believed to primarily reside within L2/3 and to a lesser extent in L5 (Yorke Jr. and Caviness Jr. 1975; Ramos, Tam, and Brumberg 2008; Fame, MacDonald, and Macklis 2011; Pal, Lim, and Richards 2024). From an anatomical organization perspective, this would be designated as predominantly feedforward (Markov *et al.* 2013; Markov and Kennedy 2013; Markov *et al.* 2014). We find however that L2/3 dominates the projection from the least number of cortical areas. Rather for the majority of areas, L6 emerges as a major source of both the intra and especially the interhemispheric projection (Olavarria and Van Sluyters 1983; Liang *et al.* 2021; Yao *et al.* 2022), regardless of the target area. This observation implies that the vast majority of cortical projections to primary sensory and motor regions are rather predominantly feedback in nature. One explanation regarding the apparent discrepancy in these two sets of observations may be due to technical differences and limitations of different tracing approaches. Chemical or protein-based anterograde and retrograde tracers such as Cholera toxin subunit B have been widely used but have low transduction efficiency (Saleeba *et al.* 2019; Weiler *et al.* 2024) compared to recently developed retrograde viruses (Tervo *et al.* 2016). Secondly, mouse cre lines are a common tool for targeting specific cells in specific layers (Bortone, Olsen, and Scanziani 2014; Harris *et al.* 2019; Yao *et al.* 2022). However, as is the case for L6 corticocortical cells (Vélez-Fort

et al. 2014), not all cell types are accessible using cre-driver lines. In our study we targeted all cell types located throughout all laminae within the target area in contrast to previous tracing studies that appear biased towards upper layers of the target area (Chovsepian *et al.* 2017; Massé *et al.* 2017; Adaikkan *et al.* 2022).

The idea that cortical feedforward and feedback circuits may have an anatomical signature has been extensively interrogated in the mammalian visual cortical system (Felleman and Van Essen 1991; Markov *et al.* 2014; Harris *et al.* 2019; D'Souza *et al.* 2022; Yao *et al.* 2022) where there exists a plethora of physiological data indicating functional hierarchy. In primates, feedforward and feedback neurons tend to reside in different cortical layers (Markov *et al.* 2014) and the ratio of supragranular to infragranular neurons has been employed to anatomically define visual cortical hierarchy (Barone *et al.* 2000; Markov *et al.* 2014).
Here we demonstrate that the fILN metric effectively ranks higher visual areas that is consistent with the anatomical organization derived from axon termination patterns, as well as retrograde rabies tracing (Harris *et al.* 2019; D'Souza *et al.* 2022; Yao *et al.* 2022) and physiological experiments that describe functional hierarchy in mice (Siegle *et al.* 2021; D'Souza *et al.* 2022; Jia *et al.* 2022). By applying fILN-based area ranking cortex-wide, we uncover a global organization that is largely consistent with the hierarchical ranking of cortical areas based on anterograde labeling (Harris *et al.* 2019), placing sensory-motor modules at the bottom and lateral, medial and prefrontal modules at the top of cortical hierarchy. Our data therefore demonstrate that the fILN metric can serve as a continuous parameter whose ranking may be used as an estimate of hierarchical dominance for understanding cortical connectivity.

Typically, feedforward projections are characterized as "drivers" while feedback projections are seen as "modulators" of neuronal activity (Markov *et al.* 2013). Our anatomical data reveal that VISp, SSp-bfd and MOp mostly receive ipsilateral feedback input from other cortical areas. This is generally expected as these targets are the first cortical areas to receive sensory input or to initiate motor functions. The predominance of feedback projections suggests a modulatory role rather than driving input onto these primary cortical areas. From our data, the pairwise intrahemispheric connectivity between VISp and SSp-bfd aligns well with historical theories of cortical hierarchy, which suggest that feedforward connections are typically complemented by reciprocal feedback connections, at least within the ipsilateral hemisphere (Felleman and Van Essen 1991; Markov *et al.* 2013; Young *et al.* 2021; Angelucci and Petreanu 2023). Our data also reveal a novel finding and notable exception that appears to involve ipsilateral primary and higher visual cortical areas providing feedforward input onto SSp-bfd. On the other hand, input from the same areas on the contralateral side are feedback in their organization as one might expect to observe for higher order areas. The fact that regardless of the target area contralateral projections are predominantly feedback suggest that the conventional rule of reciprocally feedforward and feedback projections does not apply for interhemispheric input at least to primary areas VISp, SSp-bfd or MOp.

Due to their dominant feedback bias, contralateral inputs may act as modulators of cortical activity in their ipsilateral target regions (Markov *et al.* 2014; Innocenti *et al.* 2022). For instance, inactivation of contralateral somatosensory areas in monkeys increases the receptive field size in the ipsilateral somatosensory area, suggesting a loss of modulatory contralateral input (Clarey, Tweedale, and Calford 1996). Moreover, contralateral auditory projections act to sharpen frequency tuning in its ipsilateral counterpart (Slater and Isaacson 2020) and activation of contralateral visual projections strongly modulates visual cortical responses in the binocular zone of VISp (Zhao, Liu, and Cang 2013). However, these studies purely focused on homotopic connections while the functions of heterotopic connections largely remain elusive. Given the observed extent of heterotopic connections,

future studies should address their functional roles in hemispheric communication and ultimately in behavior.

By showing that hierarchical disparities between the two hemispheres are largely accounted for by differences in the input from the sensory-motor modules, we offer a more nuanced understanding of interhemispheric communication and a prominent role for L6 that is strategically positioned within the cortex. Additionally, we show that increased fILN is predominantly due to the target areas receiving input from L6 CCs rather than L6 corticothalamic cells. L6 CCs not only integrate input from and output to its local cortical column (Vélez-Fort *et al.* 2014) but also receive substantial thalamic input, at least in sensory areas (Crandall *et al.* 2017). Moreover, responses of L6 CCs to external stimuli temporally precedes those in other cortical layers (Egger *et al.* 2020). Thus, L6 CCs are ideal candidates to rapidly relay information to other cortical areas thereby providing feedback modulation (Weiler *et al.* 2024), suggestive of predictive coding (Rao and Ballard 1999; Keller and Mrsic-Flogel 2018) or the transmission of efference copies (Holst and Mittelstaedt 1950; Latash 2021; Vallortigara 2021).

4 Methods

Animals All experiments were performed on 6–23 week old mice. For the data presented in Figures 1-6, 18 mice were used from which 11 were males and 7 were females. From these 18 mice 14 were wild type C57BL/6J mice, three were Gad2tm2(cre)Zjh/J (GAD-cre) and one mouse was B6.FVB(Cg)-Tg(Ntsr1-cre)Gn220Gsat/Mmucd (Ntsr1-cre). The GAD-cre and NTSr1-cre mice were crossed with B6.Cg-GT(ROSA)26 Sortm14(CAG-tdTomato)Hze/J (Ai14, Cre-dependent tdTomato reporter) to achieve TdTomato reporter mice. Additionally, three Ntsr1-cre x Ai14 and three GAD-cre x Ai14 mice were used for the data presented in Fig.S4. Mice were raised in standard cages on a 12 h light/dark cycle, with food and water available ad libitum. In this study, 6 VISp-injected mice were previously used to quantify areal input from the ipsilateral hemisphere (Weiler *et al.* 2024).
All surgeries and experiments were conducted in accordance with the UK Home Office regulations (Animal (Scientific Procedures) Act 1986), approved by the Animal Welfare and Ethical Review Body (AWERB; Sainsbury Wellcome Centre for Neural Circuits and Behavior) and in compliance with ARRIVE guidelines. Every effort was made to minimize the number of animals and their suffering.

Surgical procedures and viral injections All surgical procedures were carried out under isoflurane (2%–5%) and after carprofen (5 mg/kg, s.c.) had been administered. For retrograde viral tracing, we used rAAV2-retro-EF1a-H2B-EGFP (Nuclear retro-AAV, titer: 8.8 x 1013 GC per ml). Mice were anesthetized under isoflurane (2%) and craniotomies performed. Virus injection was performed using borosilicate glass injection pipettes (Wiretrol II; Drummond Scientific) pulled to a taper length of 30 mm and a tip diameter of 50 µm. Virus was delivered at a rate of 1–2 nl/s using Nanoject III (Drummond Scientific, USA) and injected at three cortical depths covering all layers of the VISp, SSp-bfd and MOp respectively (Fig.S3). After injections, the craniotomy was sealed with silicon (kwik-cast), the skin was re-sutured and animals were allowed to recover for 2–4 weeks. Injection coordinates for the monocular and binocular zone of VISp, SSp-bfd and MOp were based on the Allen Reference Atlas (coronal, 2D, Wang *et al.* 2020, see injection locations in Fig.S2,S3).

Perfusion and brain extraction For perfusions, mice were first deeply anesthetized using Pentobarbital Sodium (10 mg/kg). A blunt needle was placed in the left ventricle, whilst an incision was performed in the right atrium of the heart. Following this, blood was first cleared using 100 mM PBS. Subsequently, the animal was perfused with saline containing 4% PFA. After successful fixation, the head was removed and the brain dissected out. The brain was further fixed in 4% PFA overnight at 4 °C, and then stored in 100 mM PBS at 4 °C until ready for imaging.

Brain wide serial two-photon imaging For serial section two-photon imaging, on the day of imaging, brains were removed from the PBS and dried. Brains were then embedded in agarose (4%) using a custom alignment mold to ensure that the brain was perpendicular to the imaging axis. The agarose block containing the brains were trimmed and then mounted onto the serial two photon microscope containing an integrated vibrating microtome and motorized x–y–z stage (STP tomography, Ragan *et al.* 2012; Osten and Margrie 2013). For this, a custom system controlled by ScanImage (v5.6, Vidrio Technologies, USA) using BakingTray (https://bakingtray.mouse.vision/) was used. Imaging was performed using 920 nm illumination. Images were acquired with a 2.3 x 2.3 μm pixel size, and 5 μm plane spacing. 8-10 optical planes were acquired over a depth of 50 μm in total. To image the entire brain, images were acquired as tiles and then stitched using StitchIt (https://doi.org/10.5281/zenodo.3941901). After each mosaic tile was imaged at all optical planes, the microtome automatically cut a 50 μm slice, enabling imaging of the subsequent portions of the sample and resulting in full 3D imaging of entire brains. All images were saved as a series of 2D TIFF files. Images were registered to the Allen Mouse Brain Common Coordinate Framework (Wang *et al.* 2020) using the software brainreg (Tyson *et al.* 2022) based on the

aMAP algorithm (Niedworok *et al.* 2016). All atlas data were provided by the BrainGlobe Atlas API (Claudi *et al.* 2020). For registration, the sample image data was initially down-sampled to the voxel spacing of the atlas used and reoriented to align with the atlas orientation using bg-space (https://doi.org/10.5281/zenodo.4552537). The 10 μm atlas was used for cell detection and mapping. To manually segment viral injection sites, the software brainreg-segment (Tyson *et al.* 2022) was used. Automated cell detection and deep learning based cell classification was performed using the cellfinder software (Tyson *et al.* 2021) and cross-validated with manual annotation (see validation in Weiler *et al.* 2024). All analysis in this manuscript was performed in atlas space (Wang *et al.* 2020).Figures showing detected cells in 3D atlas space were generated using the brainrender software (Claudi *et al.* 2021) and custom scripts written in Python 3.9.

Confocal imaging and analysis For a subset of Ntsr1-cre x Ai14 and GAD-cre x Ai14, slices cut with STP topography were kept, post-fixed and mounted for confocal imaging (Leica SP8). Individual slices were imaged using tile-scan acquisitions with a 10x air objective. Voxel sizes were 2 μm (x/y) and 3-6 μm (z). We performed sequential imaging of GFP and td-tomato signals to achieve optimal spectral separation. We counted the overlap between GAD+ or NSTR1+ and retro-GFP+ cells using the Cell Counter feature of Fiji. Within the data set only approximately 1% of retro-GFP+ cells were GAD+ (Fig.S4) with no overlap between retro-GFP+ and NSTR1+ cells (Fig.S4).

Data analysis Cellfinder outputs a CSV file containing the laminar count of detected nuclei for each cortical area. This was analyzed using custom-written code in MATLAB 2023-24 and Python 3.9. We applied the following criteria for data exclusion: 1) Instances where more than 30% of the viral injection bolus was located outside the respective target area (VISp, SSp-bfd or MOp, Fig. S2A-D). 2) A given cortical area in a given hemisphere had to contain 10 or more cells. In the case where a given area contained less than 10 cells the area cell was set at zero. 3) Additionally to be included in the analysis a given area had to contain more than 10 cells in at least three injections and in the same hemisphere of three different mice. For comparison of the laminar distribution of cells within different brain areas, values were normalized to the total number of cells detected in each area. The fILN was calculated as following:

$$fILN = (L5_{fraction\ area} + L6_{fraction\ area}) / (L2/3_{fraction\ area} + L5_{fraction\ area} + L6_{fraction\ area})$$

Statistics Details of all n numbers and statistical analysis are provided either in the results and/or in the figure captions. Before comparison of data, individual data sets were checked for normality using the Anderson-Darling test in MATLAB 2023-24. The required sample sizes were estimated based on literature and our past experience performing similar experiments (Brown *et al.* 2021; Weiler *et al.* 2024). Significance level was typically set as $p<0.05$ if not stated otherwise. Statistical analyses were performed using MATLAB 2023-24. Asterisks indicate significance values as follows: *$p<0.05$, **$p<0.01$, ***$p<0.001$.

5 Author Contributions

S.W., M.T. and T.W.M conceived the project. S.W. performed all tracing and imaging experiments. S.W. and M.T. analyzed all data. M.T., T.W.M and S.W. interpreted and discussed all data and wrote the manuscript.

Acknowledgments

We thank Panagiota Iordanidou for excellent technical support and assistance as well as Mateo Vélez-Fort for comments on the manuscript. The authors are further grateful to the support staff of the Neurobiological Research Facility at Sainsbury Wellcome Centre. T.W.M. and S.W. are funded by The Wellcome Trust (214333/Z/18/Z; 090843/F/09/Z) and Humboldt Foundation (S.W.). M.T. is funded by the Interdisciplinary Centre for Clinical Research (IZKF; Advance medical scientist - Program 11).

Data, Materials, and Software Availability

Analysis code and structure of processed data will be deposited upon acceptance of this manuscript. Data available on request.

References

Adaikkan, C., J. Wang, K. Abdelaal, S. J. Middleton, P. L. Bozzelli, I. R. Wickersham, T. J. McHugh, and L.-H. Tsai. 2022. "Alterations in a cross-hemispheric circuit associates with novelty discrimination deficits in mouse models of neurodegeneration." *Neuron* 110 (19): 3091–3105.e9.

Ährlund-Richter, S., Y. Xuan, J. A. van Lunteren, H. Kim, C. Ortiz, I. Pollak Dorocic, K. Meletis, and M. Carlén. 2019. "A whole-brain atlas of monosynaptic input targeting four different cell types in the medial prefrontal cortex of the mouse." *Nature Neuroscience* 22 (4): 657–668.

Angelucci, A., and L. Petreanu. 2023. "Feedforward and Feedback Connections: Functional Connectivity, Synaptic Physiology, and Function." In *The Cerebral Cortex and Thalamus,* edited by A. Angelucci, W. M. Usrey, and S. M. Sherman, 0. Oxford University Press.

Barone, P., A. Batardiere, K. Knoblauch, and H. Kennedy. 2000. "Laminar distribution of neurons in extrastriate areas projecting to visual areas V1 and V4 correlates with the hiearchical rank and intimates the operation of a distance rule." *Journal of Neuroscience* 20 (9): 3263–3281.

Bastos, A. M., J. Vezoli, C. A. Bosman, J.-M. Schoffelen, R. Oostenveld, J. R. Dowdall, P. De Weerd, H. Kennedy, and P. Fries. 2015. "Visual Areas Exert Feedforward and Feedback Influences through Distinct Frequency Channels." *Neuron* 85 (2): 390–401.

Berezovskii, V. K., J. J. Nassi, and R. T. Born. 2011. "Segregation of feedforward and feedback projections in mouse visual cortex." *Journal of Comparative Neurology* 519 (18): 3672–3683.

Bortone, D. S., S. R. Olsen, and M. Scanziani. 2014. "Translaminar Inhibitory Cells Recruited by Layer 6 Corticothalamic Neurons Suppress Visual Cortex." *Neuron* 82 (2): 474–485.

Brown, A. P. Y., L. Cossell, M. Strom, A. L. Tyson, M. Vélez-Fort, and T. W. Margrie. 2021. "Analysis of segmentation ontology reveals the similarities and differences in connectivity onto L2/3 neurons in mouse V1." *Scientific Reports* 11 (1): 4983.

Buffalo, E. A., P. Fries, R. Landman, T. J. Buschman, and R. Desimone. 2011. "Laminar differences in gamma and alpha coherence in the ventral stream." *Proceedings of the National Academy of Sciences* 108 (27): 11262–11267.

Chovsepian, A., L. Empl, D. Correa, and F. M. Bareyre. 2017. "Heterotopic transcallosal projections are present throughout the mouse cortex." *Frontiers in Cellular Neuroscience* 11 (February): 1–12.

Clarey, J. C., R. Tweedale, and M. B. Calford. 1996. "Interhemispheric modulation of somatosensory receptive fields: evidence for plasticity in primary somatosensory cortex." *Cerebral Cortex* 6 (2): 196–206.

Claudi, F., L. Petrucco, A. L. Tyson, T. Branco, T. W. Margrie, and R. Portugues. 2020. "BrainGlobe Atlas API: a common interface for neuroanatomical atlases." *Journal of Open Source Software* 5 (54): 2668.

Claudi, F., A. L. Tyson, L. Petrucco, T. W. Margrie, R. Portugues, and T. Branco. 2021. "Visualizing anatomically registered data with brainrender." *eLife* 10:e65751.

Crandall, S. R., S. L. Patrick, S. J. Cruikshank, and B. W. Connors. 2017. "Infrabarrels Are Layer 6 Circuit Modules in the Barrel Cortex that Link Long-Range Inputs and Outputs." *Cell Reports* 21 (11): 3065–3078.

D'Souza, R. D., Q. Wang, W. Ji, A. M. Meier, H. Kennedy, K. Knoblauch, and A. Burkhalter. 2022. "Hierarchical and nonhierarchical features of the mouse visual cortical network." *Nature Communications* 13 (1): 503.

Egger, R., R. T. Narayanan, J. M. Guest, A. Bast, D. Udvary, L. F. Messore, S. Das, C. P. J. de Kock, and M. Oberlaender. 2020. "Cortical Output Is Gated by Horizontally Projecting Neurons in the Deep Layers." *Neuron* 105 (1): 122–137.e8.

Fame, R. M., J. L. MacDonald, and J. D. Macklis. 2011. "Development, specification, and diversity of callosal projection neurons." *Trends in Neurosciences* 34 (1): 41–50.

Felleman, D. J., and D. C. Van Essen. 1991. “Distributed Hierarchical Processing in the Primate Cerebral Cortex.” *Cerebral Cortex* 1 (1): 1–47.

Fenlon, L. R., and L. J. Richards. 2015. “Contralateral targeting of the corpus callosum in normal and pathological brain function.” *Trends in Neurosciences* 38 (5): 264–272.

Gazzaniga, M. S. 2000. “Cerebral specialization and interhemispheric communication: Does the corpus callosum enable the human condition?” *Brain* 123 (7): 1293–1326.

Goulas, A., H. B. M. Uylings, and C. C. Hilgetag. 2017. “Principles of ipsilateral and contralateral cortico-cortical connectivity in the mouse.” *Brain Structure and Function* 222 (3): 1281–1295.

Hafner, G., M. Witte, J. Guy, N. Subhashini, L. E. Fenno, C. Ramakrishnan, Y. S. Kim, *et al.* 2019. “Mapping Brain-Wide Afferent Inputs of Parvalbumin-Expressing GABAergic Neurons in Barrel Cortex Reveals Local and Long-Range Circuit Motifs.” *Cell Reports* 28 (13): 3450–3461.e8.

Harris, J. A., S. Mihalas, K. E. Hirokawa, J. D. Whitesell, H. Choi, A. Bernard, P. Bohn, *et al.* 2019. “Hierarchical organization of cortical and thalamic connectivity.” *Nature* 575 (7781): 195–202.

Holst, E. von, and H. Mittelstaedt. 1950. “Das Reafferenzprinzip.” *Naturwissenschaften* 37 (20): 464–476.

Innocenti, G. M., K. Schmidt, C. Milleret, M. Fabri, M. G. Knyazeva, A. Battaglia-Mayer, F. Aboitiz, *et al.* 2022. “The functional characterization of callosal connections.” *Progress in Neurobiology* 208:102186.

Jia, X., J. H. Siegle, S. Durand, G. Heller, T. K. Ramirez, C. Koch, and S. R. Olsen. 2022. “Multi-regional module-based signal transmission in mouse visual cortex.” *Neuron* 110 (9): 1585–1598.e9.

Keller, G. B., and T. D. Mrsic-Flogel. 2018. “Predictive Processing: A Canonical Cortical Computation.” *Neuron* 100 (2): 424–435.

Latash, M. L. 2021. “Efference copy in kinesthetic perception: a copy of what is it?” *Journal of Neurophysiology* 125 (4): 1079–1094.

Leinweber, M., D. R. Ward, J. M. Sobczak, A. Attinger, and G. B. Keller. 2017. “A Sensorimotor Circuit in Mouse Cortex for Visual Flow Predictions.” *Neuron* 95 (6): 1420–1432.e5.

Liang, Y., J. L. Fan, W. Sun, R. Lu, M. Chen, and N. Ji. 2021. “A Distinct Population of L6 Neurons in Mouse V1 Mediate Cross-Callosal Communication.” *Cerebral Cortex* 31 (9): 4259–4273.

Markov, N. T., and H. Kennedy. 2013. “The importance of being hierarchical.” *Current Opinion in Neurobiology* 23 (2).

Markov, N. T., M. Ercsey-Ravasz, D. C. Van Essen, K. Knoblauch, Z. Toroczkai, and H. Kennedy. 2013. “Cortical High-Density Counterstream Architectures.” *Science* 342 (6158): 1238406.

Markov, N. T., J. Vezoli, P. Chameau, A. Falchier, R. Quilodran, C. Huissoud, C. Lamy, *et al.* 2014. “Anatomy of hierarchy: Feedforward and feedback pathways in macaque visual cortex.” *Journal of Comparative Neurology* 522 (1): 225–259.

Marques, T., J. Nguyen, G. Fioreze, and L. Petreanu. 2018. “The functional organization of cortical feedback inputs to primary visual cortex.” *Nature Neuroscience* 21 (5): 757–764.

Massé, I. O., S. Ross, G. Bronchti, and D. Boire. 2017. “Asymmetric Direct Reciprocal Connections Between Primary Visual and Somatosensory Cortices of the Mouse.” *Cerebral Cortex* 27 (9): 4361–4378.

Mumford, D. 1992. “On the computational architecture of the neocortex.” *Biological Cybernetics* 66 (3): 241–251.

Muñoz-Castañeda, R., B. Zingg, K. S. Matho, X. Chen, Q. Wang, N. N. Foster, A. Li, *et al.* 2021. “Cellular anatomy of the mouse primary motor cortex.” *Nature* 598 (7879): 159–166.

Niedworok, C. J., A. P. Brown, M. Jorge Cardoso, P. Osten, S. Ourselin, M. Modat, and T. W. Margrie. 2016. “aMAP is a validated pipeline for registration and segmentation of high-resolution mouse brain data.” *Nature Communications 2016 7:1* 7 (1): 1–9.

Ocklenburg, S., and Z. V. Guo. 2024. “Cross-hemispheric communication: Insights on lateralized brain functions.” *Neuron* 112 (8): 1222–1234.

Olavarria, J., and R. C. Van Sluyters. 1983. “Widespread callosal connections in infragranular visual cortex of the rat.” *Brain Research* 279 (1-2): 233–237.

Osten, P., and T. W. Margrie. 2013. “Mapping brain circuitry with a light microscope.” Publisher: Nature Publishing Group, *Nature Methods* 10 (6): 515–523.

Pal, S., J. W. C. Lim, and L. J. Richards. 2024. “Diverse axonal morphologies of individual callosal projection neurons reveal new insights into brain connectivity.” *Current Opinion in Neurobiology* 84 (102837).

Ragan, T., L. R. Kadiri, K. U. Venkataraju, K. Bahlmann, J. Sutin, J. Taranda, I. Arganda-Carreras, Y. Kim, H. S. Seung, and P. Osten. 2012. “Serial two-photon tomography for automated ex vivo mouse brain imaging.” *Nature Methods* 9 (3): 255–258.

Ramos, R. L., D. M. Tam, and J. C. Brumberg. 2008. “Physiology and morphology of callosal projection neurons in mouse.” *Neuroscience* 153 (3): 654–63.

Rao, R. P. N., and D. H. Ballard. 1999. “Predictive coding in the visual cortex: a functional interpretation of some extra-classical receptive-field effects.” *Nature Neuroscience* 2 (1): 79–87.

Rockland, K. S., and D. N. Pandya. 1979. “Laminar origins and terminations of cortical connections of the occipital lobe in the rhesus monkey.” *Brain Research* 179 (1): 3–20.

Saleeba, C., B. Dempsey, S. Le, A. Goodchild, and S. McMullan. 2019. “A student’s guide to neural circuit tracing.” *Frontiers in Neuroscience* 13:897.

Siegle, J. H., X. Jia, S. Durand, S. Gale, C. Bennett, N. Graddis, G. Heller, *et al.* 2021. “Survey of spiking in the mouse visual system reveals functional hierarchy.” *Nature* 592 (7852): 86–92.

Slater, B. J., and J. S. Isaacson. 2020. “Interhemispheric callosal projections sharpen frequency tuning and enforce response fidelity in primary auditory cortex.” *eNeuro* 7 (4): 1–11.

Sun, Q., X. Li, M. Ren, M. Zhao, Q. Zhong, Y. Ren, P. Luo, *et al.* 2019. “A whole-brain map of long-range inputs to GABAergic interneurons in the mouse medial prefrontal cortex.” *Nature Neuroscience* 22 (8): 1357–1370.

Swanson, L. W., J. D. Hahn, and O. Sporns. 2017. “Organizing principles for the cerebral cortex network of commissural and association connections.” *Proceedings of the National Academy of Sciences* 114 (45): E9692–E9701.

Szczupak, D., P. M. Iack, D. Rayêe, C. Liu, R. Lent, F. Tovar-Moll, and A. C. Silva. 2023. “The relevance of heterotopic callosal fibers to interhemispheric connectivity of the mammalian brain.” *Cerebral Cortex* 33 (8): 4752–4760.

Teichert, M., and J. Bolz. 2018. “How Senses Work Together: Cross-Modal Interactions between Primary Sensory Cortices.” *Neural Plasticity* 2018:e5380921.

Tervo, D. G. R., B.-Y. Hwang, S. Viswanathan, T. Gaj, M. Lavzin, K. D. Ritola, S. Lindo, *et al.* 2016. “A Designer AAV Variant Permits Efficient Retrograde Access to Projection Neurons.” *Neuron* 92 (2): 372–382.

Tyson, A. L., C. V. Rousseau, C. J. Niedworok, S. Keshavarzi, C. Tsitoura, L. Cossell, M. Strom, and T. W. Margrie. 2021. “A deep learning algorithm for 3D cell detection in whole mouse brain image datasets.” *PLOS Computational Biology* 17 (5): e1009074.

Tyson, A. L., M. Vélez-Fort, C. V. Rousseau, L. Cossell, C. Tsitoura, S. C. Lenzi, H. A. Obenhaus, F. Claudi, T. Branco, and T. W. Margrie. 2022. "Accurate determination of marker location within whole-brain microscopy images." *Scientific Reports 2022 12:1* 12 (1): 1–8.

Vallortigara, G. 2021. "The Efference Copy Signal as a Key Mechanism for Consciousness." *Frontiers in Systems Neuroscience* 15.

Vélez-Fort, M., C. V. Rousseau, C. J. Niedworok, I. R. Wickersham, E. A. Rancz, A. P. Brown, M. Strom, and T. W. Margrie. 2014. "The Stimulus Selectivity and Connectivity of Layer Six Principal Cells Reveals Cortical Microcircuits Underlying Visual Processing." *Neuron* 83 (6): 1431–1443.

Vezoli, J., L. Magrou, R. Goebel, X.-J. Wang, K. Knoblauch, M. Vinck, and H. Kennedy. 2021. "Cortical hierarchy, dual counterstream architecture and the importance of top-down generative networks." *NeuroImage* 225:117479.

Wang, Q., S. L. Ding, Y. Li, J. Royall, D. Feng, P. Lesnar, N. Graddis, *et al.* 2020. "The Allen Mouse Brain Common Coordinate Framework: A 3D Reference Atlas." *Cell* 181 (4): 936–953.e20.

Weiler, S., V. Rahmati, M. Isstas, J. Wutke, A. W. Stark, C. Franke, J. Graf, *et al.* 2024. "A primary sensory cortical interareal feedforward inhibitory circuit for tacto-visual integration." *Nature Communications* 15 (1): 3081.

Xu, N.-l., M. T. Harnett, S. R. Williams, D. Huber, D. H. O'Connor, K. Svoboda, and J. C. Magee. 2012. "Nonlinear dendritic integration of sensory and motor input during an active sensing task." *Nature* 492 (7428): 247–251.

Yao, S., Q. Wang, K. E. Hirokawa, B. Ouellette, R. Ahmed, J. Bomben, K. Brouner, *et al.* 2022. "A whole-brain monosynaptic input connectome to neuron classes in mouse visual cortex." *Nature Neuroscience,* 1–15.

Yorke Jr., C. H., and V. S. Caviness Jr. 1975. "Interhemispheric neocortical connections of the corpus callosum in the normal mouse: A study based on anterograde and retrograde methods." *Journal of Comparative Neurology* 164 (2): 233–245.

Young, H., B. Belbut, M. Baeta, and L. Petreanu. 2021. "Laminar-specific cortico-cortical loops in mouse visual cortex." *eLife* 10:1–25.

Zhang, S., M. Xu, T. Kamigaki, J. P. Hoang Do, W.-C. Chang, S. Jenvay, K. Miyamichi, L. Luo, and Y. Dan. 2014. "Long-range and local circuits for top-down modulation of visual cortex processing." *Science* 345 (6197): 660–665.

Zhao, X., M. Liu, and J. Cang. 2013. "Sublinear binocular integration preserves orientation selectivity in mouse visual cortex." Publisher: Nature Publishing Group, *Nature Communications* 4 (1): 2088.

Zhou, J., Y. Wen, L. She, Y.-n. Sui, L. Liu, L. J. Richards, and M.-m. Poo. 2013. "Axon position within the corpus callosum determines contralateral cortical projection." *Proceedings of the National Academy of Sciences* 110 (29): E2714–E2723.